Noninvasive Electric Current Induction for Low-Frequency Tissue Conductivity Reconstruction: Is It Feasible With a TMS-MRI Setup?

Stefano Mandija[1], Petar I. Petrov[2], Sebastian F. W. Neggers[2], Peter R. Luijten[1,3], and Cornelis A. T. van den Berg[1,4]

[1]Center for Image Sciences, University Medical Center Utrecht, Utrecht, The Netherlands; [2]Rudolf Magnus Institute of Neuroscience, University Medical Center Utrecht, Utrecht, The Netherlands; [3]Department of Radiology, University Medical Center Utrecht, Utrecht, The Netherlands; and [4]Department of Radiotherapy, University Medical Center Utrecht, Utrecht, The Netherlands

Corresponding Author:
Stefano Mandija
Center for Image Sciences, University Medical Center Utrecht,
Heidelberglaan 100, 3584 CX, E01.132, Utrecht, The Netherlands,
E-mail: S.Mandija@umcutrecht.nl

Key Words: low frequency, conductivity, TMS-MRI, MR phase maps

Abbreviations: Magnetic resonance (MR), transcranial magnetic stimulation (TMS), magnetic resonance imaging (MRI), low frequency (LF), electromagnetic (EM), MR-electrical impedance tomography (MR-EIT), radiofrequency (RF), signal-to-noise ratio (SNR)

ABSTRACT

Noninvasive quantification of subject-specific low-frequency brain tissue conductivity (σ_{LF}) will be valuable in different fields, for example, neuroscience. Magnetic resonance (MR)-electrical impedance tomography allows measurements of σ_{LF}. However, the required high level of direct current injection leads to an undesirable pain sensation. Following the same principles, but avoiding pain sensation, we evaluate the feasibility of inductively inducing currents using a transcranial magnetic stimulation (TMS) device and recording the magnetic field variations arising from the induced tissue eddy currents using a standard 3 T MR scanner. Using simulations, we characterize the strength of the incident TMS magnetic field arising from the current running in the TMS coil, the strength of the induced magnetic field arising from the induced currents in tissues by TMS pulses, and the MR phase accuracy required to measure this latter magnetic field containing information about σ_{LF}. Then, using TMS-MRI measurements, we evaluate the achievable phase accuracy for a typical TMS-MRI setup. From measurements and simulations, it is crucial to discriminate the incident from the induced magnetic field. The incident TMS magnetic field range is $\pm 10^{-4}$ T, measurable with standard MR scanners. In contrast, the induced TMS magnetic field is much weaker ($\pm 10^{-8}$ T), leading to an MR phase contribution of $\sim 10^{-4}$ rad. This phase range is too small to be measured, as the phase accuracy for TMS-MRI experiments is $\sim 10^{-2}$ rads. Thus, although highly attractive, noninvasive measurements of the induced TMS magnetic field, and therefore estimations of σ_{LF}, are experimentally not feasible.

INTRODUCTION

Noninvasive mapping of tissue electrical properties in the megahertz range has recently become feasible with the development of magnetic resonance imaging (MRI)-based electrical property tomography (1-5). However, precise knowledge on tissue electrical conductivity at low frequency (LF: Hz–100 kHz) and the relation between electrical conduction and tissue composition in this frequency range is still limited. In the kilohertz range, the human body is electrically very heterogeneous (6-8) as cellular fraction, water-ionic content, and cell membranes modulate electrical conductivity. Unfortunately, pathologies change these factors, causing differences in tissue conductivity values (σ_{LF}) between healthy and nonhealthy subjects (9, 10). The ability to measure these subject-specific σ_{LF} values of brain tissues is particularly a desired competence in neuroscience, as various diagnostic techniques and neurostimulation modalities like transcranial magnetic stimulation (TMS) operate in this frequency range (11-14).

TMS is an emerging technique that allows noninvasive modulation of cortical neurophysiology to diagnose and treat neurological disorders (15-20). Based on the Faraday induction principle, TMS uses a strong, time-varying magnetic field to inductively induce an electric field in the brain that can cause neuroactivation (Figure 1A) (21-24). Practically, TMS dosimetry is performed in a highly empirical fashion by using the "motor threshold" method (20, 23), where the motor cortex serves as

ISSN 2379-1381 http://dx.doi.org/10.18383/j.tom.2016.00232

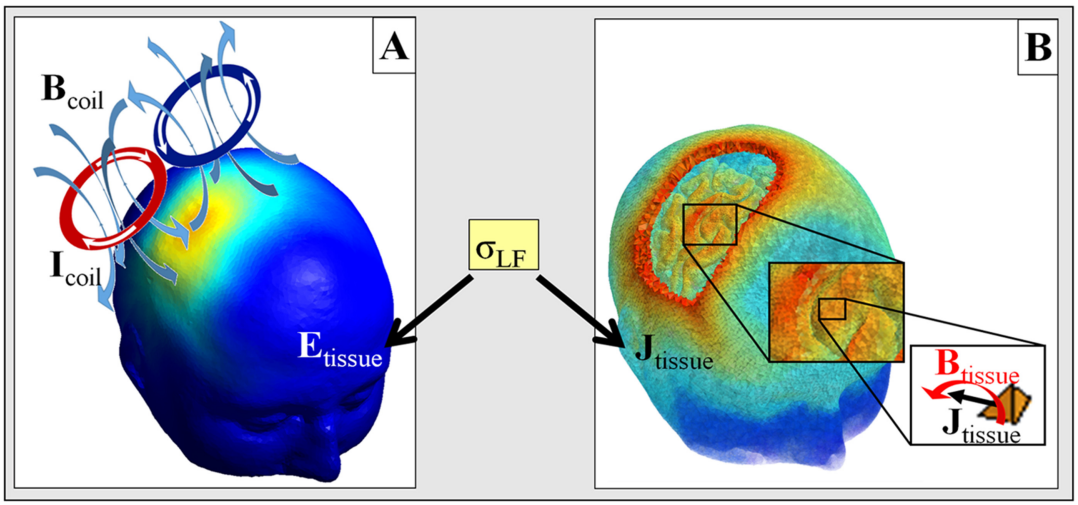

Figure 1. A time-varying current (I_{coil}) running in a figure-8-shaped TMS coil creates a time-varying magnetic field ($\mathbf{B}_{coil}$) which, in turn, induces an electric field ($\mathbf{E}_{tissue}$) in brain tissues (A). Because of the conductive nature (σ_{LF}) of brain tissues, induced currents ($\mathbf{J}_{tissue}$) arise from $\mathbf{E}_{tissue}$ (B). These induced currents create an induced magnetic field ($\mathbf{B}_{tissue}$). Information on low-frequency (LF) tissue conductivity σ_{LF} is, therefore, imprinted only in $\mathbf{B}_{tissue}$ and not in $\mathbf{B}_{coil}$.

reference area. However, because the electric field induced in the brain is modulated by the varying dielectric properties and the gyrification of the cortex (25, 26), the TMS dose varies for brain regions that are different from the motor cortex (27-30). Therefore, the motor threshold method is unreliable for most TMS purposes (31-33).

To precisely guide TMS administration and to better understand the behavioral consequences of the deployed TMS electric field, different research groups are focusing their investigations on how stimulation parameters (number of TMS pulses, pulses' strength, coil models, and orientation) affect the induced TMS electric field by means of electromagnetic (EM) simulations (34-39). Although these valuable studies correctly adopt heterogeneous conductive brain models in the computation of the induced TMS electric field, the adopted conductivity values are simply derived from healthy group averages (40-42). Unfortunately, as argued in other studies (24, 30, 43-46), healthy group averages of σ_{LF} cannot ensure optimal subject-specific dosimetry, as various factors such as ageing (47) and pathologies (10) induce variations in σ_{LF} values. Moreover, because the induced electric field is also modulated by the tissue geometry, having subject-specific brain models would be valuable (32, 44, 48). Although this latter requirement can be satisfied by segmenting magnetic resonance (MR) images acquired before TMS administration, being able to noninvasively and nonpainfully determine subject-specific tissue σ_{LF} values is still an unresolved issue.

LF tissue conductivity can be mapped using MR-electrical impedance tomography (MR-EIT) (49-51). In this technique, strong direct current (10 mA) is injected into the brain via skin surface electrodes (Figure 2A) while the subject is positioned in an MR scanner. The spatial pattern of these currents is modulated by the underlying tissue σ_{LF} distribution. In turn, these injected currents lead to an induced magnetic field, in which information on σ_{LF} is thus imprinted. By measuring this induced magnetic field using MR phase measurements, σ_{LF} maps can be reconstructed (52, 53). However, strong currents and long injection times (10 milliseconds) are needed to achieve adequate MR phase accuracy in MR-EIT experiments. These requirements result in a sensation of pain that limits the in vivo applicability of MR-EIT.

To map tissue σ_{LF} by avoiding direct current injection, using time-varying magnetic fields created by external coils to inductively induce currents has been suggested (Figure 1B and Figure 2B) (54). Subsequently, by following this inductive fashion, directly using the MR gradient coils to induce currents (55-57) has been suggested. Thus, high current density at injection points and, thus, pain sensation are avoided, making this approach very attractive and applicable to standard clinical MR scanners. However, tissue σ_{LF} reconstructions were not feasible. In fact, the phase contribution arising from the induced magnetic field is too small to be accurately measured with standard MR systems (58, 59). In addition, it has also been shown that subtle, unavoidable imaging distortions hamper measurements of this phase contribution by creating a pseudo-LF conductivity contrast (60).

By following the appealing idea of inductively inducing currents in tissues, in this study, we use a TMS setup to induce much stronger currents (Figure 1A) in combination with an MR scanner used to measure the arising induced magnetic field (Figure 1B). Moreover, while standard MR gradient coils allow slew rates of 20 T/s at 10 cm from the gradients' isocenter, a TMS device can generate slew rates of up to 20 000 T/s. Thus, the reported 3 orders of magnitude increase that are needed to measure the induced magnetic field could be theoretically achieved (59). We have divided this study in 2 parts. First, using simulations, we characterize the strength of the induced magnetic field carrying information on the induced currents in the

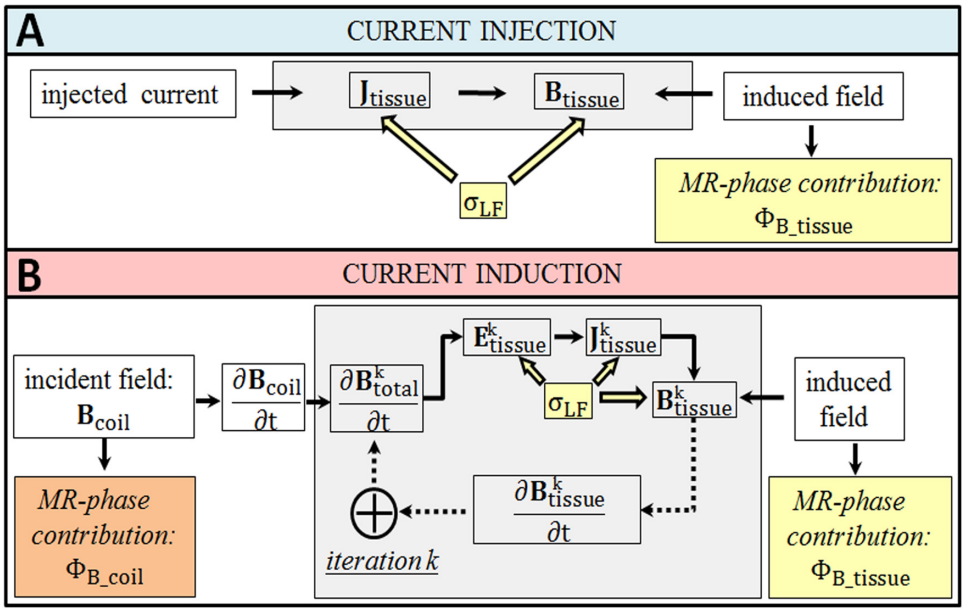

Figure 2. Current injection: the additional magnetic resonance (MR) phase contribution (Φ_{B_tissue}) contains information on LF tissue conductivity (A). Current induction—quasi-static approximation: 2 additional MR phase contributions (B). Φ_{B_coil} does not carry any information about σ_{LF}. Instead, Φ_{B_tissue} contains information about σ_{LF}, as for the case of current injection.

tissue and, thus, the LF conductivity and compare with that of the incident TMS magnetic field. This was evaluated for different conductive cylindrical models and realistic human brain models. Thus, we characterize the required phase accuracy to detect these induced magnetic fields with MRI. Moreover, we study the impact of different TMS waveforms. Second, MR measurements on phantoms are presented to investigate the achievable phase accuracy for a typical TMS-MRI setup. With this study, we investigate whether inductively inducing currents in tissues by using a TMS-MRI setup is a feasible methodology for performing noninvasive LF tissue conductivity reconstructions.

THEORY

In TMS, the presence of conductive tissues such as the brain underneath the TMS coil leads to correction terms in the computation of the TMS EM field, which are a function of the tissue conductivity distribution (Figure 2B). In this kilohertz range, where displacement currents are negligible, these corrections can be modeled by the so-called quasi-static approximation (35). For this purpose, Maxwell equations are expanded in power series in the frequency domain ($\mathbf{E} = \Sigma_{k=0}^{\infty} (j\omega)^k \mathbf{E}^{[k]}$ and $\mathbf{B} = \Sigma_{k=0}^{\infty} (j\omega)^k \mathbf{B}^{[k]}$), giving the following relations for a k^{th} order (61):

$$\nabla \times \mathbf{E}^{[k]} = -\frac{\partial \mathbf{B}^{[k-1]}}{\partial t} \quad (1)$$

$$\mathbf{J}^{[k]} = \sigma_{LF} \mathbf{E}^{[k]} \quad (2)$$

$$\nabla \times \mathbf{B}^{[k]} = \mu_0 \mathbf{J}^{[k]} \quad (3)$$

where a quasi-static condition is assumed in equation (2) (35, 62). For readability purposes, we do not explicitly write the spatial dependency (r) of the vector fields. In addition, the conductivity σ_{LF} is also a tensor because of tissue anisotropy, but we can consider it as a scalar value for simplicity of derivation. From equation (3), the Biot–Savart law can be derived as follows:

$$\mathbf{B}^{[k]} = \frac{\mu_0}{4\pi} \int_v \frac{\mathbf{J}^{[k]} \times (\mathbf{r} - \mathbf{r}_0)}{|\mathbf{r} - \mathbf{r}_0|^3} dV_0. \quad (4)$$

In TMS, for $k = 0$, the zero-order vectors in the brain/object satisfy the static field equations $\nabla \times \mathbf{E}^{[0]} = 0$, $\mathbf{E}^{[0]} = 0$, $\nabla \times \mathbf{B}^{[0]} = 0$, $\nabla \cdot \mathbf{B}^{[0]} = 0$. $\mathbf{B}^{[0]}$ is the incident TMS magnetic field arising from the current running in the TMS coil, thus not carrying any information about tissue conductivity. Throughout the paper, we will refer to this magnetic field as $\mathbf{B}_{coil}$ as follows:

$$\mathbf{B}^{[0]} = \mathbf{B}_{coil} \quad (5)$$

which gives an MR phase contributions defined as Φ_{B_coil} (63).

Higher-order field corrections of order k can be computed using the vectors of order k - 1 as sources (Figure 2B). For $k = 1$, the following equations are computed:

$$\nabla \times \mathbf{E}^{[1]} = \frac{\partial \mathbf{B}^{[0]}}{\partial t} = -\frac{\partial \mathbf{B}_{coil}}{\partial t} \quad (6)$$

$$\mathbf{J}^{[1]} = \sigma_{LF} \mathbf{E}^{[1]} \quad (7)$$

$$\nabla \times \mathbf{B}^{[1]} = \mu_0 \mathbf{J}^{[1]} \quad (8)$$

$$\mathbf{B}^{[1]} = \frac{\mu_0}{4\pi} \int_v \frac{\mathbf{J}^{[1]} \times (\mathbf{r} - \mathbf{r}_0)}{|\mathbf{r} - \mathbf{r}_0|^3} dV_0 \quad (9)$$

where $\mathbf{E}^{[1]}$ and $\mathbf{J}^{[1]}$ are, respectively, the first-order electric field and current density induced in a conductive domain such as the brain, and $\mathbf{B}^{[1]}$ is the first-order induced magnetic field arising from $\mathbf{J}^{[1]}$. Therefore, information on tissue conductivity is imprinted in $\mathbf{B}^{[1]}$.

The total induced electric field in brain tissues, called as $\mathbf{E}_{tissue}$ throughout the paper, is:

$$\mathbf{E}_{tissue} = \sum_{k=1}^{\infty} \mathbf{E}^{[k]}. \quad (10)$$

In principle, E_{tissue} is a solenoidal electric field induced by the time-varying incident TMS magnetic field B_{coil} [equation (6)]. However, because of the nonhomogeneous conductivity distribution of brain tissues, charge is accumulated at the boundaries between different conductive structures, leading to a conservative electric field that affects the incident, solenoidal electric field (25, 35, 48) as follows:

$$E_{tissue} = E_{solenoidal} + E_{conservative} \quad (11)$$

$E_{solenoidal}$ is proportional to the time-varying incident vector potential A_{coil}, which depends solely on the TMS coil configuration and level of current running into it $\left(E_{solenoidal} = -\frac{\partial A_{coil}}{\partial t}\right)$. Thus, $E_{solenoidal}$ is always present, independently from the conductor underneath the TMS coil. Instead, $E_{conservative}$, which arises from the charge accumulation at tissue boundaries between different conductive tissues ($E_{conservative} = -\nabla\varphi$, with φ electrical potential), is directly modulated by the underlying tissue geometry and conductivity distribution σ_{LF} (25, 35, 48). From equation (2), the total induced current density in tissue, called as J_{tissue}, is, therefore, $J_{tissue} = \sigma_{LF}E_{tissue}$.

Analogous to equation (10), the total induced TMS magnetic field, called as B_{tissue}, is:

$$B_{tissue} = \sum_{k=1}^{\infty} B^{[k]} \quad (12)$$

which gives an MR phase contributions defined as Φ_{B_tissue}.

By combining equations (5) and (12), the total TMS magnetic field is, therefore, defined as follows:

$$B_{total} = \sum_{k=0}^{\infty} B^{[k]} = B^{[0]} + \sum_{k=1}^{\infty} B^{[k]} = B_{coil} + B_{tissue}. \quad (13)$$

MATERIALS AND METHODS

Simulations

EM simulations aimed to characterize the strength of the incident and the induced TMS magnetic fields (B_{coil} and B_{tissue}, respectively) by using the quasi-static approximation described in the theory section. We then assessed the phase accuracy needed to detect Φ_{B_tissue} in concurrent TMS-MRI experiments. In addition, we characterized the impact of different conductivity distributions of σ_{LF} on B_{tissue}.

Three simulations were performed in SCIRun (64), namely, 2 on conductive cylinders and 1 on a realistic human brain model. For the performed simulations, the TMS coil was modeled using 2 single-plane spiral wings (65), reflecting the geometry of the TMS coil used in the measurements. These wings were placed at 5 cm from the cylinders to mimic the actual position used in the measurements and in contact with the scalp to mimic the position in realistic TMS treatments.

In the first simulation, we characterized the strength of the z-component of the net (time average over the TMS pulse) incident TMS magnetic field B_{coil_z}, the only 1 component (parallel to the MR static magnetic field B0) measurable in an MR experiment. We also characterized the range of the net phase contribution Φ_{B_coil} that would arise from B_{coil_z} in an MR experiment. In an MR experiment, the phase contribution Φ_{B_coil} is proportional to the area underneath the TMS current waveform (63). The same phase contribution can be obtained by using the time average value of the TMS current waveform (see online supplemental Appendix A, $\overline{I_{coil}}$) computed from independent oscilloscope measurements. For this simulation, a typical bipolar TMS pulse that lasts for a full period was used (Figure 3A). The TMS output was set to 1%, leading to a $\overline{I_{coil}} = 3.5$ A. By applying the Biot–Savart law, the net B_{coil_z} was computed. This simulation was performed using a homogeneous conductive cylinder (Figure 4A) with the same geometry and electric conductivity as that of the phantom used in the measurements (Figure 4D). Thus, consistent comparison with measurements could be performed. However, for a bipolar TMS pulse that lasts for a full period, the net induced current in tissue $\overline{J_{tissue}}$ is zero (see online supplemental Appendix A and Figure 3B) (66). Thus, obviously, the induced magnetic field B_{tissue_z} and its related phase contribution Φ_{B_tissue} are zero.

Because information on σ_{LF} is imprinted solely in B_{tissue}, to induce a non-zero net B_{tissue_z}, a truncated TMS waveform should be used (see online supplemental Appendix A and Figure 3, case 2). Consequently, in the second simulation, we used the same waveform adopted in the first simulation but truncated at the first quarter (63), TMS output 1%, and $t_1 = 0.1$ ms, leading to $\overline{I_{coil}} = 35$ A and a rate of change of the coil current of 0.55×10^6 A, in line with other studies (36, 42). We characterized the strength of the net B_{coil_z} and Φ_{B_coil} for such a truncated TMS pulse. Then, the 3-dimensional mesh model, the conductivity distribution, and the vector potential (computed using the rate of change of the coil current) (35) were given as input to the finite element method (FEM) solver to compute E_{tissue} and J_{tissue}. From J_{tissue}, the strength of B_{tissue_z} and the range of Φ_{B_tissue} were characterized. By performing this simulation on 2 different conductive cylinders (one homogeneous and one consisting of 2 different conducting compartments, (Figure 4, A and B) (67), the impact of different conductive compartments was evaluated.

Then, in the third simulation, we defined the strength of B_{coil_z} and B_{tissue_z} for realistic in vivo situations by using a realistic human brain model (68) and the truncated TMS waveform adopted in the second simulation. We, therefore, explored the feasibility of measuring Φ_{B_tissue} in vivo by characterizing the required phase accuracy for concurrent TMS-MRI experiments. In addition, we evaluated the impact of different σ_{LF} distributions on E_{tissue} (relevant quantity for TMS dosimetry) and B_{tissue}. Finally, we characterized the phase accuracy needed to detect subtle variations in B_{tissue} arising from these variations in σ_{LF}. The phase accuracy determines the feasibility of this technique. The adopted σ_{LF} values reflect the conductivity variations reported in other studies (Figure 4C) (35, 38, 42).

Measurements

Concurrent TMS-MRI measurements were conducted in a clinical 3 T MR scanner (Achieva, Philips Healthcare, Best, The Netherlands) with elliptical surface MR receive coils (flex-M) and using a standard TMS stimulator (Magstim Rapid2, Whitland, UK) with an MR-compatible figure-8-shaped TMS coil (28, 69). Using a typical TMS-MRI setup, the phase accuracy characterized by these measurements is representative.

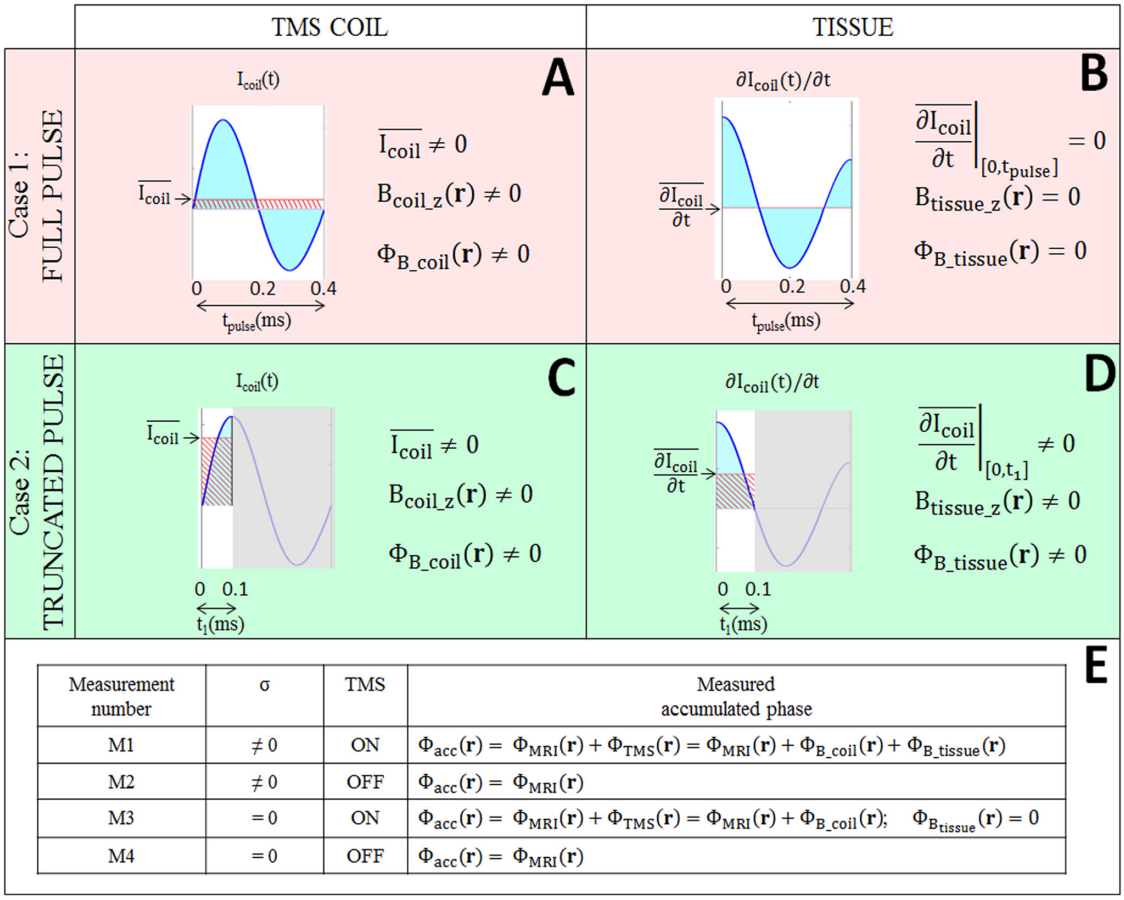

Measurement number	σ	TMS	Measured accumulated phase
M1	≠ 0	ON	$\Phi_{acc}(\mathbf{r}) = \Phi_{MRI}(\mathbf{r}) + \Phi_{TMS}(\mathbf{r}) = \Phi_{MRI}(\mathbf{r}) + \Phi_{B\_coil}(\mathbf{r}) + \Phi_{B\_tissue}(\mathbf{r})$
M2	≠ 0	OFF	$\Phi_{acc}(\mathbf{r}) = \Phi_{MRI}(\mathbf{r})$
M3	= 0	ON	$\Phi_{acc}(\mathbf{r}) = \Phi_{MRI}(\mathbf{r}) + \Phi_{TMS}(\mathbf{r}) = \Phi_{MRI}(\mathbf{r}) + \Phi_{B\_coil}(\mathbf{r})$; $\Phi_{B_{tissue}}(\mathbf{r}) = 0$
M4	= 0	OFF	$\Phi_{acc}(\mathbf{r}) = \Phi_{MRI}(\mathbf{r})$

Figure 3. Net transcranial magnetic stimulation (TMS)-coil current, net incident TMS magnetic field, and its related phase contribution for a full TMS pulse shape (A) and for a truncated TMS pulse shape (C). The pulse shape of the current running in the TMS coil was derived from oscilloscope measurements. Net time derivative of the TMS-coil current (proportional to the induced electric field), net induced TMS magnetic field, and its related phase contribution for a full TMS pulse shape (B) and for a truncated TMS pulse shape (D). Four concurrent TMS-magnetic resonance imaging (MRI) measurements (E).

The MR sequence adopted was a spin-echo sequence with the following parameters: relaxation time/echo time = 1000/50 milliseconds, field of view = 160 × 160 × 2.5 mm^3, resolution = 2.5 × 2.5 × 2.5 mm^3, voxel/bandwidth = 0.15/3 kHz, and number of signal averages = 2. The TMS device was synchronized with the MR sequence by using the MR-transistor–transistor logic signal delivered at every radiofrequency (RF) excitation as a reference time point. TMS pulses were delivered before each readout gradient (69). The surface of the TMS coil was placed at 4.5 cm from the phantoms. For each experiment, 4 measurements were performed to correctly isolate the phase contributions Φ_{B_coil} and Φ_{B_tissue} (see online supplemental Appendix B and Figure 4D, measurement numbers M1–4). For the measurements with TMS-on, the TMS outputs were 1% and 4%, for the first and the second experiments, respectively. Because a standard TMS stimulator was used, only bipolar pulses that lasted for a full period could be used (Figure 3, case 1). For these measurements, we prepared 2 agar phantoms sturdy enough to prevent motion artifacts (60) as follows: 1 conductive (1.6 S/m) and 1 nonconductive, as a reference to compensate for Φ_{B_coil} (see online supplemental Appendix B, Figure 4D). The 2 phantoms were carefully placed at the same position in the scanner by using a dedicated phantom holder designed for this purpose.

With these experiments, we characterized the phase range of Φ_{TMS}, which, in principle, includes both the contributions Φ_{B_coil} and Φ_{B_tissue}, by using the conductive phantom (see online supplemental Appendix B). We also characterized the phase range of only Φ_{B_coil} by using the nonconductive phantom. This allowed direct comparison with the first simulation. We finally characterized the achievable MR phase accuracy (inverse of the signal-to-noise ratio [SNR]) (59) to enable Φ_{B_tissue} measurements in concurrent TMS-MRI experiments for a realistic TMS-MRI setup.

RESULTS

The impact of a realistic TMS pulse shape that lasts for a full period (Figure 3, case 1) on the TMS-related phase contribution, Φ_{B_coil}, is characterized by using the homogeneous cylinder (Figure 5A). The results of this first simulation are shown on the same plane where measurements were performed, thus mimick-

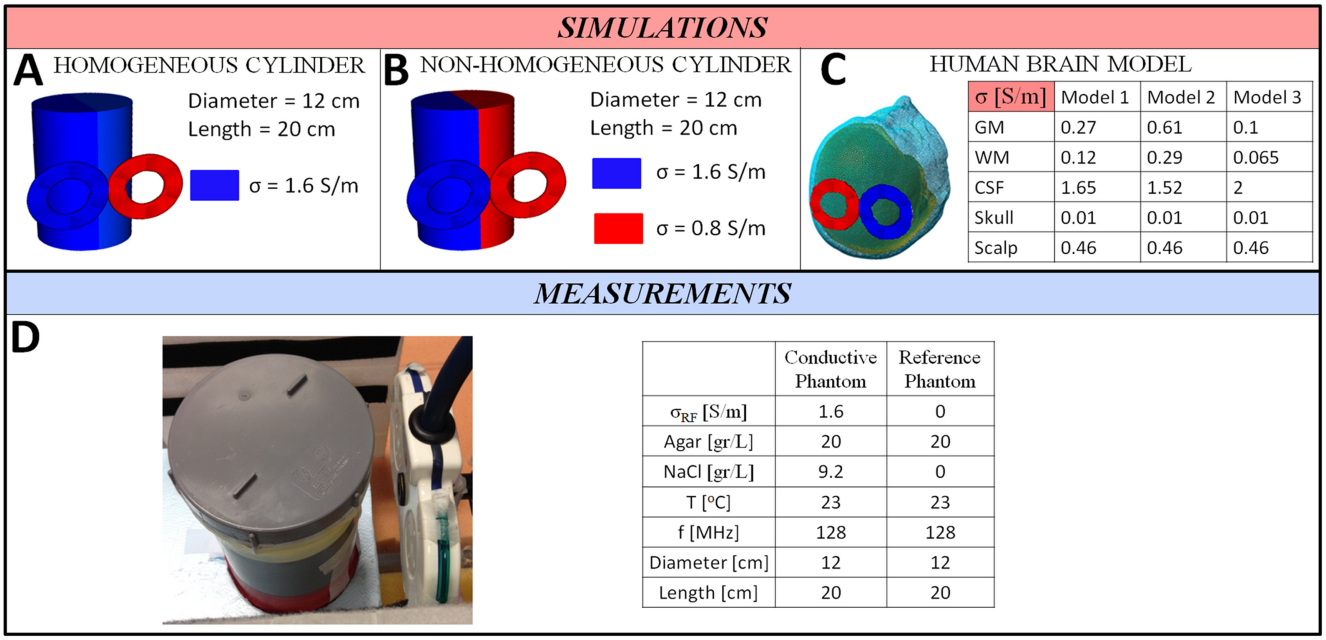

σ [S/m]	Model 1	Model 2	Model 3
GM	0.27	0.61	0.1
WM	0.12	0.29	0.065
CSF	1.65	1.52	2
Skull	0.01	0.01	0.01
Scalp	0.46	0.46	0.46

	Conductive Phantom	Reference Phantom
σ_{RF} [S/m]	1.6	0
Agar [gr/L]	20	20
NaCl [gr/L]	9.2	0
T [°C]	23	23
f [MHz]	128	128
Diameter [cm]	12	12
Length [cm]	20	20

Figure 4. Cylindrical models used in simulations: one homogeneous (A) and one with 2 compartments (B). The 3-dimensional (3D) mesh was performed using Gmsh. Realistic human brain model and 3 sets of tissue conductivity used in simulations (C). Geometry and composition of the experimental phantoms (D). Conductivity values were confirmed by dielectric probe measurements (85070E Agilent Technology, Santa Clara, California).

ing the experimental setup and allowing direct comparison with the measurements. From simulations, B_{coil_z} is on the order of 10^{-5} T (Figure 5B), leading to a Φ_{B_coil} in the order of radians (Figure 5C). This result suggests that Φ_{B_coil}, and thus B_{coil_z}, can be measured in an MR experiment.

Figure 6 shows the results from the second simulations performed on 2 conductive cylinders (one homogeneous and one with 2 different conductive compartments, Figure 6A and Figure 6F, respectively) and using the truncated TMS pulse waveform to induce a nonzero B_{tissue_z} (Figure 3, case 2). From these simulations, we observe that the use of a truncated TMS waveform leads to an increase in B_{coil_z} (10^{-4} T) and, consequently, in Φ_{B_coil} (10^2 rads), with respect to the use of a full TMS waveform (Figure 5). In addition, by comparing the results obtained from the 2 different conductive cylinders, we observe that the incident magnetic field B_{coil_z} (Figure 6, B and G) and its related phase contribution Φ_{B_coil} (Figure 6, C and H) are not affected by the presence of different conductive compartments. This is because the incident magnetic field does not depend on the conductivity of the structure underneath the TMS coil. Instead, as shown by these simulations, the conductivity distribution σ_{LF} modulates the induced magnetic field B_{tissue_z} (Figure 6, D and I) and thus its related phase contribution Φ_{B_tissue} (Figure 6, E and J). The impact of σ_{LF} variations is clearly visible from the discrepancy between the histograms of the 2 B_{tissue_z} maps (Figure 6K). However, it is important to note that the induced magnetic field B_{tissue_z} ($\sim 10^{-8}$ T) is about 4 orders of magnitude lower than the incident magnetic field B_{coil_z} (10^{-4} T). As shown in Figure 6, E and J, Φ_{B_tissue} is in the range of $\sim 10^{-4}$ rads. This result characterizes the phase accuracy needed

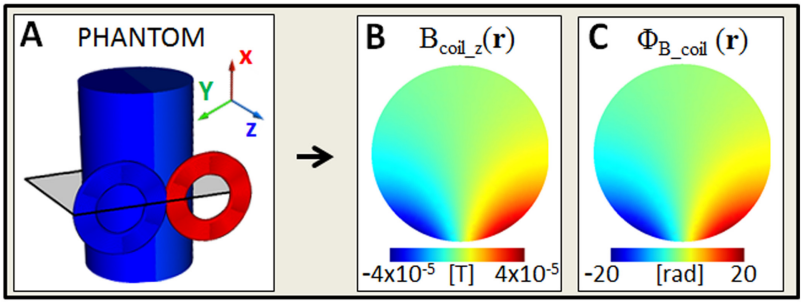

Figure 5. Phantom simulation (full TMS waveform): the displayed maps are extracted from 3D simulations on the same plane where measurements were performed. Homogeneous cylindrical model (A). z-Component of $\mathbf{B}_{coil}$ (B) and Φ_{B_coil} maps (C), both independent from the sample conductivity.

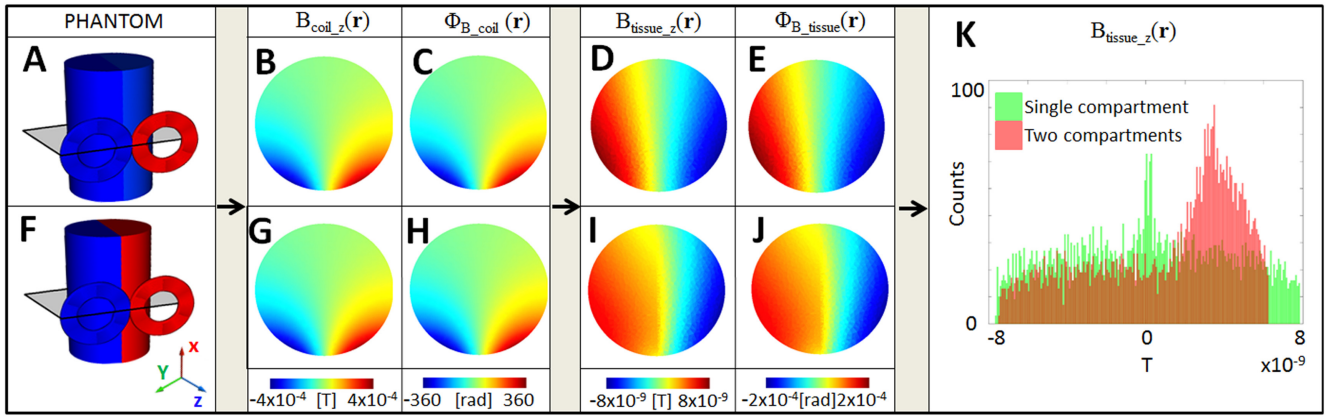

Figure 6. Phantom simulations (truncated TMS waveform). Homogeneous (A) and 2-compartment cylindrical models (F). z-Component of $\mathbf{B}_{coil}$ (B, G) and Φ_{B_coil} maps (C, H), independent from the sample conductivity. z-Component of $\mathbf{B}_{tissue}$ (D, I) and Φ_{B_tissue} maps for the 2 cylindrical models (E, J). Histograms of $\mathbf{B}_{tissue}$ for the 2 models (K). Clearly visible variation in $\mathbf{B}_{tissue}$ patterns between the 2 models.

to measure B_{tissue_z} in concurrent TMS-MRI experiments. Moreover, these results highlight the challenge of correctly disentangling the phase contributions arising from B_{coil_z} and B_{tissue_z}, as the latter field constitutes a very small fraction of the former.

In the third simulations, the impact of inter-subject variations of σ_{LF} on E_{tissue} and B_{tissue_z} and the range of B_{coil_z} and B_{tissue_z} are characterized for a realistic human brain model (Figure 7 and Figure 8, respectively). For the adopted 3 different conductive brain models, the norm of E_{tissue} is shown on the gray matter and white matter surfaces (Figure 7). Our results correspond with the results presented in a previous valuable study (35). By comparing the mean and standard deviation of the top 30% values of $\|E_{tissue}\|$ for the 3 models (calculated independently for each brain model in the gray matter and the white matter), we observe that different σ_{LF} values induce significant variations in the deployed E_{tissue} (Figure 7, bar-plots). This highlights the importance of accurately predicting subject-specific tissue conductivity values to correctly guide TMS dosimetry.

For each brain model (Figure 8A), B_{tissue_z} and the related phase contribution Φ_{B_tissue} are computed (Figure 8C). The induced magnetic field B_{tissue_z} (10^{-8} T) is about 4 orders of magnitude lower than the incident magnetic field B_{coil_z} (10^{-4} T) (Figure 8B), in line with the value observed for the cylindrical structure (Figure 6). In addition, B_{tissue_z} maps show slightly different patterns between the 3 different brain models because of the different conductivity distributions. This is a direct consequence of the previously observed variations in the E_{tissue} maps. As shown in Figure 8D, variations in σ_{LF} lead to magnetic field variations in the range of nanotesla. From these results (Figure 8C), we conclude that the necessary MR phase accuracy needed to measure Φ_{B_tissue} for in vivo TMS-MRI experiments is about 10^{-4} rads. However, an even higher accuracy will be needed to actually detect variations in tissue conductivity distributions.

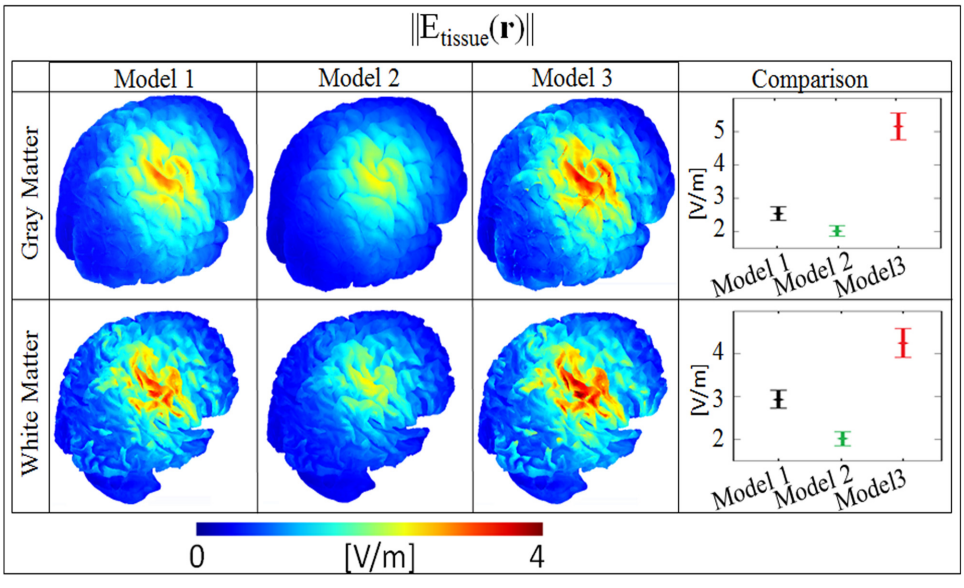

Figure 7. Norms of $\mathbf{E}_{tissue}$ in the gray matter (GM—top row) and white matter (WM— bottom row) for the 3 brain models. Mean and standard deviation of the top 30% values of the norm of $\mathbf{E}_{tissue}$ for each brain model in GM and WM. It is visible how different σ_{LF} distributions lead to significant variations in the induced electric field.

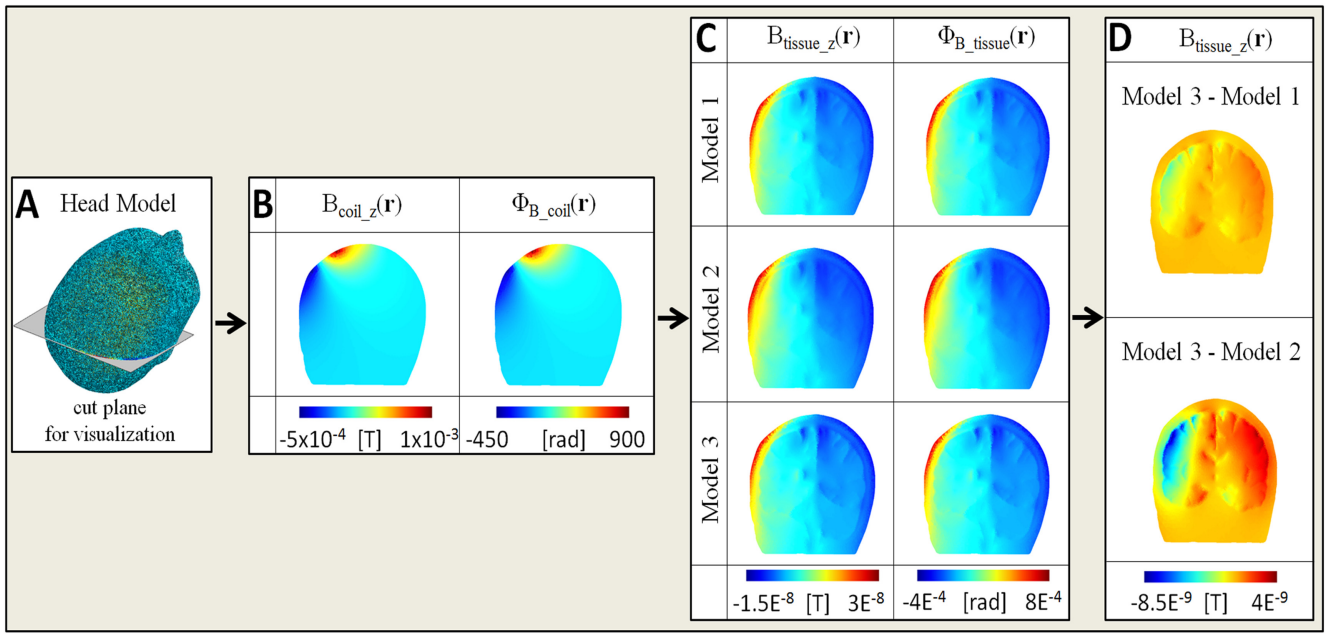

Figure 8. Realistic head model and cut plane used for visualization purposes (A). z-Component of $\mathbf{B}_{coil}$ and Φ_{B_coil} maps, both independent from σ_{LF} (B). For each model, the z-component of $\mathbf{B}_{tissue}$ and Φ_{B_tissue} is computed (C). Variations in the z-component of $\mathbf{B}_{tissue}$ because of different conductivity distributions (D). These maps were computed by subtracting $\mathbf{B}_{tissue}$ of model 3 and $\mathbf{B}_{tissue}$ of model 1 (upper part), and by subtracting $\mathbf{B}_{tissue}$ of model 3 and $\mathbf{B}_{tissue}$ of model 2 (bottom part).

In Figures 9 and 10, the results of the 2 experiments performed by using a realistic TMS-MRI setup and a full TMS waveform are proposed. With these experiments, we assess the attainable MR phase accuracy for concurrent TMS-MRI experiments. In both experiments, 2 phase maps were acquired for each phantom (one conductive and one nonconductive): one with TMS-on (Figure 9 and Figure 10, A and C) and one with TMS-off (Figure 9 and Figure 10, B and D). The significant

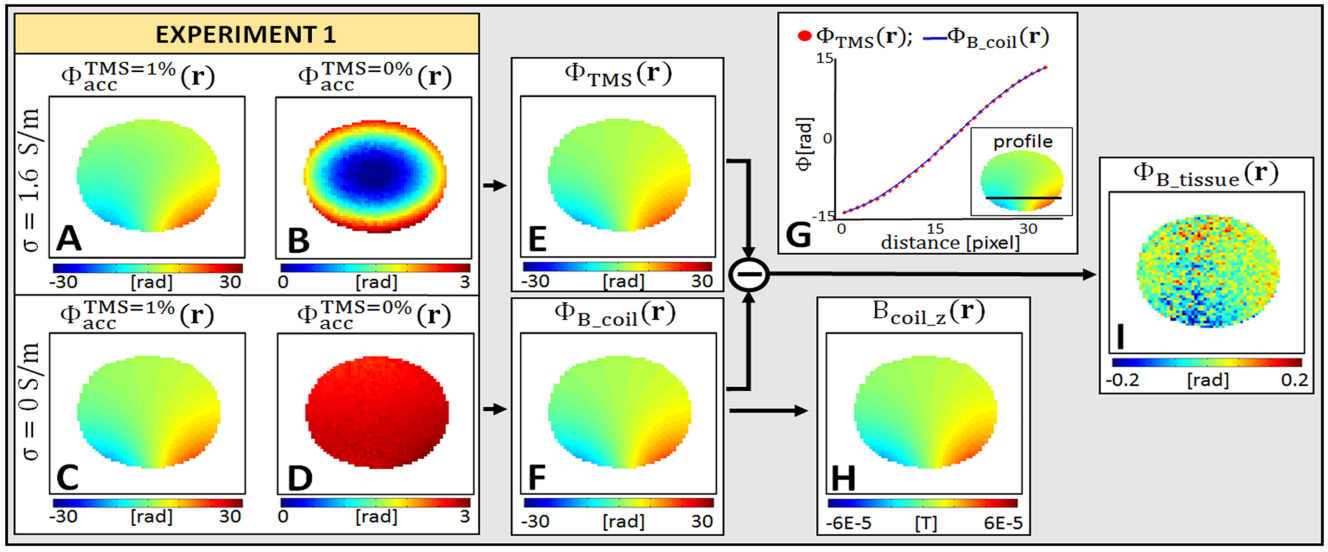

Figure 9. Experiment 1: TMS = 1%. Phase maps with TMS-on for the conductive (A) and nonconductive (C) phantoms. Phase maps with TMS-off for the conductive (B) and nonconductive (D) phantoms. Reconstructed Φ_{TMS} map for the conductive phantom (E). Reconstructed Φ_{B_coil} map for the reference phantom (F). Comparison between Φ_{TMS} and Φ_{B_coil} profiles (G). Reconstructed B_{coil_z} map (H). Φ_{B_tissue} map (subtraction between Φ_{TMS} and Φ_{B_coil}) (I).

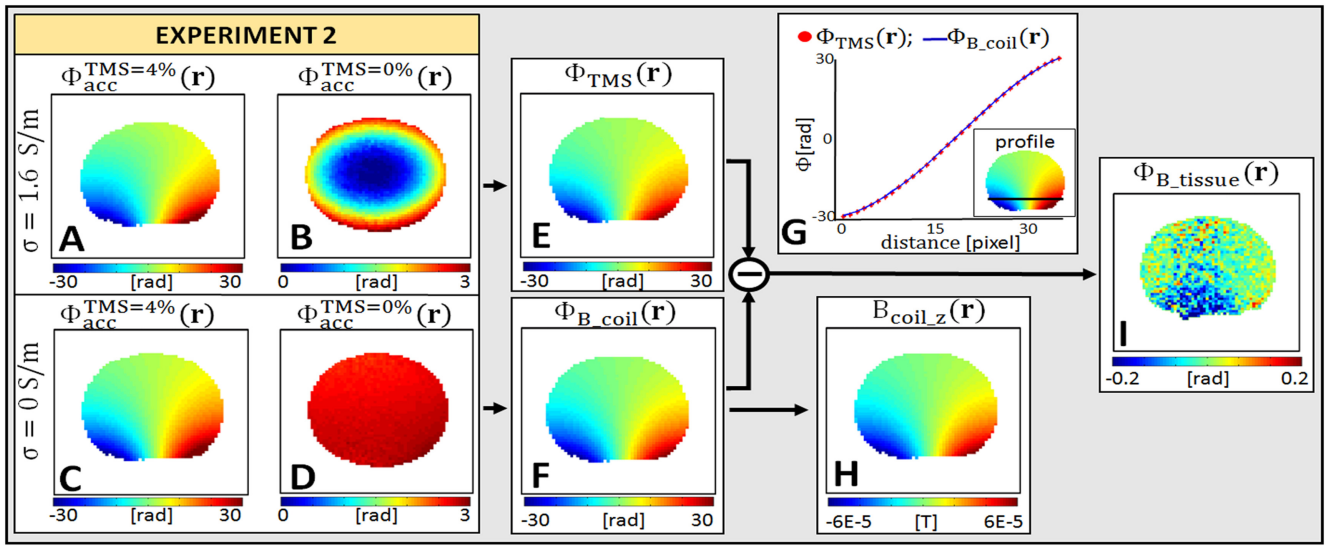

Figure 10. Experiment 2: TMS = 4%. Phase maps with TMS-on for the conductive (A) and nonconductive (C) phantoms. Phase maps with TMS-off for the conductive (B) and nonconductive (D) phantoms. Reconstructed Φ_{TMS} map for the conductive phantom (E). Reconstructed Φ_{B_coil} map for the reference phantom (F). Comparison between Φ_{TMS} and Φ_{B_coil} profiles (G). Reconstructed B_{coil_z} map (H). Φ_{B_tissue} map (subtraction between Φ_{TMS} and Φ_{B_coil}) (I).

impact of different Φ_{RF} (RF phase contribution, ~3 rads, see online supplemental Appendix B), which scales with the RF conductivity (megahertz), is visible in the measurements with TMS-off. This highlights the importance of correctly compensating for Φ_{RF}. By subtracting the phase maps measured with TMS-on and TMS-off [subtraction inside parentheses in equation (B.2); see online supplemental Appendix B], Φ_{TMS} (Figure 9E and Figure 10E) and Φ_{B_coil} (Figure 9F and Figure 10F) are computed, respectively, for the conductive and the nonconductive phantoms. As shown in the plots (Figure 9G and Figure 10G), Φ_{TMS} coincides with Φ_{B_coil}. From Φ_{B_coil} maps, the z-component of B_{coil} is reconstructed (Figure 9H and Figure 10H). The range of the measured Φ_{B_coil} (radians) and B_{coil_z} (10^{-5} T) quantitatively reflects the values previously observed in simulations. Finally, Φ_{B_tissue} maps can be, in principle, obtained by subtracting Φ_{TMS} and Φ_{B_coil} maps [see online supplemental Appendix B, subtraction between parentheses in equation (B.2)] (Figure 9I and Figure 10I).

For the performed measurements, the actual MR phase accuracy for Φ_{B_tissue} detection is estimated to be in the order of 10^{-2} rad, which is 2 orders higher than what is required from simulations. In addition, for the adopted full TMS waveform, we should observe that Φ_{B_tissue} is zero, as the net induced J_{tissue} is zero. However, in Φ_{B_tissue} maps, we can observe a certain pattern in the range of 0.1 rads. This pattern is caused by an imperfect compensation of Φ_{B_coil} while performing the subtraction between Φ_{TMS} and Φ_{B_coil} (relative error ~1%). Therefore, this result highlights that very high precision is required to correctly compensate for Φ_{B_coil}.

Finally, to evaluate whether a stronger net incident TMS magnetic field could be of benefit, we performed a second experiment with a TMS output of 4%. From our measurements (Figure 10), significant image corruption can be observed in the region underneath the TMS coil. This corruption arises from the intra-voxel dephasing created by the stronger incident, highly nonuniform TMS magnetic field B_{coil}.

DISCUSSION

Being able to measure subject-specific σ_{LF} would be valuable for different fields of research such as oncology and neuroscience (11-14, 70). In MR-EIT, in vivo conductivity measurements require direct injection of eddy currents in tissue and measurements of their impact on the MR phase (49-51). In this study, we explored whether inductive generation of currents using an MR-compatible TMS setup could be a less painful alternative to MR-EIT. Such a setup is able to generate much stronger time-varying magnetic fields than switching MR gradient coils previously proposed in other studies (58-60). However, as shown by our analysis, 3 main challenges hamper measurements of the induced magnetic field arising from inductively induced currents in tissues.

First, for such an inductive technique to work, it is crucial to correctly disentangle the incident magnetic field from the induced magnetic field. This is because, only this latter field contains information on tissue σ_{LF}. For this purpose, subtractions between different phase images are needed (see online supplemental Appendix B). The fundamental problem is that the induced magnetic field B_{tissue} is about 10^{-4} lower that the incident magnetic field B_{coil}. Therefore, very high precision and reproducibility is required to correctly disentangle the phase contribution Φ_{B_tissue} arising from B_{tissue} from the phase contribution Φ_{B_coil} arising from B_{coil}.

Second, as demonstrated, information on σ_{LF} is only imprinted in B_{tissue}. Therefore, to reconstruct σ_{LF}, the net B_{tissue} has to be nonzero. As discussed in this work, this requirement is satisfied if a truncated TMS pulse is used. However, for standard TMS setups, only TMS pulses that last for a full period can be used; thus, the net B_{tissue} is zero (see online supplemental Appendix A, Figure 3, case 1) (66).

Therefore, an additional setup (pulse modulator) should be used to comply with this requirement.

Third, supposing that it would be possible to correctly isolate Φ_{B_tissue} from all the other phase contributions, from our simulations, the phase range of Φ_{B_tissue} is in the order of 10^{-4} rads. This phase range is about 2 orders of magnitude lower than the detectable phase in concurrent TMS-MRI experiments. In addition, to distinguish small variations in tissue conductivity, an even higher phase accuracy would be needed.

To bring Φ_{B_tissue} into a measurable phase range, one should increase B_{tissue} of at least 2 orders of magnitude. To strengthen B_{tissue}, one can increase the strength of the induced current J_{tissue} by increasing the TMS pulse frequency and pulse strength.

By increasing the pulse frequency, that is, reducing the induction time (t_i), stronger J_{tissue} and, therefore, B_{tissue} can be achieved. In contrast, attention has to be paid to not enter into a different dispersion band. Brain tissues exhibit the beta dispersion centered between 10^5–10^7 Hz. Above this dispersion band (100 MHz), the cell membranes exhibit a negligible impedance, so currents are capable of passing through both the extracellular and intracellular media (71). To avoid conductivity reconstructions in a different frequency dispersion band, and thus not directly translatable to LF tissue conductivity, the TMS-pulse frequency (1–10 kHz) can be increased by an additional factor of 10 (ie, t_i = 0.01 milliseconds). However, in an MRI experiment, the measured net Φ_{B_tissue} is proportional to both B_{tissue_z} and the induction time t_i. Hence, in the computation of Φ_{B_tissue}, the increase in B_{tissue_z} is cancelled by the reduction in the induction time t_i, leading to an unchanged Φ_{B_tissue} range. For this reason, the increase of the TMS-pulse frequency would not be a beneficial solution.

As aforementioned, another strategy to increase the induced J_{tissue} can be to strengthen the TMS output. B_{tissue} increases with a stronger TMS output, but B_{coil} also increases. Unfortunately, as already observed in Figure 10, this leads to considerable signal dephasing. From our results, a truncated TMS pulse and much stronger TMS outputs should be used to bring Φ_{B_tissue} above the noise level. To comply with such a requirement, one should measure a much stronger, highly nonuniform Φ_{B_coil}. Consequently, to avoid signal dephasing, one should therefore considerably reduce the voxel size (in the range of micrometers).

This latter observation brings us to a final consideration. A smaller voxel size comes quickly at the cost of SNR loss. Instead, to detect very small magnetic field fluctuations such as the one produced by B_{tissue}, the SNR should be considerably increased. Thus, only the number of scan repetitions can be increased. However, in practice, unfeasible scan time would be required to achieve enough SNR for Φ_{B_tissue} measurements.

As discussed, the unsuccessful ability to measure B_{tissue} by inductively inducing currents in the brain using a combined TMS-MRI setup arises from the physical limitations behind the physics of the induction principle. On the contrary, by injecting currents in tissues (MR-EIT), direct measurements of B_{tissue} and, consequently, σ_{LF} reconstructions are feasible. The first macroscopic difference between the 2 techniques is that in MR-EIT, images subtractions between different conductive phantoms are not needed. This is because currents are directly injected into the brain, thus there is no incident magnetic field B_{coil}. Second, for both techniques, Φ_{B_tissue} is proportional to B_{tissue_z} and to t_i, time of injection/induction. Despite the comparable B_{tissue_z} range ($\pm 10^{-8}$ T), the relevant difference in the time of injection/induction (10 milliseconds in MR-EIT and 0.1 milliseconds in TMS-MRI) leads to a measurable/nonmeasurable Φ_{B_tissue} in MR-EIT and TMS-MRI, respectively (72).

These observations define the physical limitations hampering the feasibility of noninvasively measuring subject-specific σ_{LF}. Hence, future studies should focus on alternative methodologies to noninvasively and nonpainfully measure B_{tissue} for subject-specific σ_{LF} reconstructions.

CONCLUSIONS

LF tissue conductivity σ_{LF} reconstructions can only be performed by measuring the phase contribution arising from the induced magnetic field, in which information on σ_{LF} is imprinted. However, despite stronger currents being inductively induced using a TMS stimulator compared with MR gradient coils, these measurements are not feasible with a standard TMS-MRI setup. This is because, the induced magnetic field is very weak; thus, very high SNR is required to correctly measure it. If a higher level of current running through the TMS coil is used to strengthen the induced currents in tissues and to increase the induced magnetic field, considerable image dephasing would be observed because of the strong, highly nonuniform incident TMS magnetic field. In light of our observations, we believe that direct σ_{LF} reconstructions performed by inductively inducing currents in the brain are not feasible even if a TMS-MRI setup is used.

Supplemental Materials

Supplemental Appendix A–B: http://dx.doi.org/10.18383/j.tom.2016.00232.s01

ACKNOWLEDGMENTS

This work was supported by the DeNeCor project being part of the ENIAC Joint Undertaking.

REFERENCES

1. Voigt T, Katscher U, Doessel O. Quantitative conductivity and permittivity imaging of the human brain using electric properties tomography. Magn Reson Med. 2011;66(2):456–466.
2. Sodickson DK, Alon L, Deniz CM, Brown R, Zhang B, Wiggins GC, Cho GY, Eliezer NB, Novikov DS, Lattanzi R, Duan Q, Sodickson LA, Zhu Y. Local Maxwell Tomography using transmit-receive coil arrays for contact-free mapping of tissue electrical properties and determination of absolute RF phase. Paper presented at ISMRM 20th Annual Meeting; May 2012; Melbourne, Australia.
3. van Lier AL, Brunner DO, Pruessmann KP, Klomp DW, Luijten PR, Lagendijk JJ, van den Berg CA. B1+ phase mapping at 7 T and its application for in vivo electrical conductivity mapping. Magn Reson Med. 2012;67(2):552–561.
4. Lee J, Shin J, Kim D. MR-based conductivity imaging using multiple receiver coils. Magn Reson Med. 2015;75(2):530–539.
5. Liu J, Zhang X, Schmitter S, Van de Moortele PF, He B. Gradient-based electrical properties tomography (gEPT): A robust method for mapping electrical properties

of biological tissues in vivo using magnetic resonance imaging. Magn Reson Med. 2015;74(3):634–646.
6. Pethig R. Dielectric properties of biological materials: biophysical and medical applications. IEEE Trans Dielectr Electr Insul. 1984;EI-19(5):453–474.
7. Gabriel S, Lau RW, Gabriel C. The dielectric properties of biological tissues: II. Measurements in the frequency range 10 Hz to 20 GHz. Phys Med Biol. 1996; 41(11):2251–2269.
8. Gabriel C, Peyman A, Grant EH. Electrical conductivity of tissue at frequencies below 1 MHz. Phys Med Biol. 2009;54(16):4863–4878.
9. Gullmar D, Haueisen J, Reichenbach JR. Influence of anisotropic electrical conductivity in white matter tissue on the EEG[Sweta]MEG forward and inverse solution. A high-resolution whole head simulation study. Neuroimage. 2010: 51:145–163.
10. Jochmann T, Güllmar D, Haueisen J, Reichenbach JR. Influence of tissue conductivity changes on the EEG signal in the human brain: a simulation study. Z Med Phys. 2011;21(2):102–112.
11. Ilmoniemi RJ, Kicić D. Methodology for combined TMS and EEG. Brain Topogr. 2010;22(4):233–248.
12. Harvey BM, Vansteensel MJ, Ferrier CH, Petridou N, Zuiderbaan W, Aarnoutse EJ, Bleichner MG, Dijkerman HC, van Zandvoort MJ, Leijten FS, Ramsey NF, Dumoulin SO. Frequency specific spatial interactions in human electrocorticography: V1 alpha oscillations reflect surround suppression. Neuroimage. 2013;65:424–432.
13. de Berker AO, Bikson M, Bestmann S. Predicting the behavioral impact of transcranial direct current stimulation: issues and limitations. Front Hum Neurosci. 2013;7:613.
14. Peters JC, Reithler J, Schuhmann T, de Graaf T, Uludag K, Goebel R, Sack AT. On the feasibility of concurrent human TMS-EEG-fMRI measurements. J Neurophysiol. 2013;109(4):1214–1227.
15. Hummel FC, Cohen LG. Non-invasive brain stimulation: a new strategy to improve neurorehabilitation after stroke? Lancet Neurol. 2006;5(8):708–712.
16. O'Reardon JP, Solvason HB, Janicak PG, Sampson S, Isenberg KE, Nahas Z, McDonald WM, Avery D, Fitzgerald PB, Loo C, Demitrack MA, George MS, Sackeim HA. Efficacy and safety of transcranial magnetic stimulation in the acute treatment of major depression: a multisite randomized controlled trial. Biol Psychiatry. 2007;62(11):1208–1216.
17. Rossini PM, Rossi S. Transcranial magnetic stimulation: diagnostic, therapeutic, and research potential. Neurology. 2007;68(7):484–488.
18. Fregni F, Pascual-Leone A. Technology insight: noninvasive brain stimulation in neurology perspectives on the therapeutic potential of rTMS and tDCS. Nat Clin Pract Neurol. 2007;3(7):383–393.
19. Pollak TA, Nicholson TR, Edwards MJ, David AS. A systematic review of transcranial magnetic stimulation in the treatment of functional (conversion) neurological symptoms. J Neurol Neurosurg Psychiatry. 2014;85(2):191–197.
20. Rossini PM, Burke D, Chen R, Cohen LG, Daskalakis Z, Di Iorio R, Di Lazzaro V, Ferreri F, Fitzgerald PB, George MS, Hallett M, Lefaucheur JP, Langguth B, Matsumoto H, Miniussi C, Nitsche MA, Pascual-Leone A, Paulus W, Rossi S, Rothwell JC, Siebner HR, Ugawa Y, Walsh V, Ziemann U. Non-invasive electrical and magnetic stimulation of the brain, spinal cord, roots and peripheral nerves: basic principles and procedures for routine clinical and research application. An updated report from an I.F.C.N. Committee. Clin Neurophysiol.2015:126(6): 1071–1107.
21. Kobayashi M, Pascual-Leone A. Transcranial magnetic stimulation in neurology. Lancet Neurol. 2003;2(3):145–156.
22. Siebner HR, Hartwigsen G, Kassuba T, Rothwell JC. How does transcranial magnetic stimulation modify neuronal activity in the brain? Implications for studies of cognition. Cortex. 2009;45(9):1035–1042.
23. Schutter DJLG, van Honk J. A standardized motor threshold estimation procedure for transcranial magnetic stimulation research. J ECT. 2006;22(6):176–178.
24. Bestmann S, de Berker AO, Bonaiuto J. Understanding the behavioural consequences of noninvasive brain stimulation. Trends Cogn Sci. 2015:19(1):75–100.
25. Roth BJ, Saypol JM, Hallett M, Cohen LG. A theoretical calculation of the electric field induced in the cortex during magnetic stimulation. Electroencephalogr Clin Neurophysiol. 1991;81(1):47–56.
26. Tofts PS, Branston NM. The measurement of electric field, and the influence of surface charge, in magnetic stimulation. Electroencephalogr Clin Neurophysiol. 1991;81(3):238–239.
27. Komssi S, Kähkönen S, Ilmoniemi RJ. The effect of stimulus intensity on brain responses evoked by transcranial magnetic stimulation. Hum Brain Mapp. 2004; 21(3):154–164.
28. de Weijer AD, Sommer IE, Bakker EJ, Bloemendaal M, Bakker CJ, Klomp DW, Bestmann S, Neggers SF. A setup for administering TMS to medial and lateral cortical areas during whole brain fMRI recording. J Clin Neurophysiol. 2014; 31(5):474–487.
29. Janssen AM, Oostendorp TF, Stegeman DF. The effect of local anatomy on the electric field induced by TMS: evaluation at 14 different target sites. Med Biol Eng Comput. 2014;52:873–883.
30. Wassermann EM. Variation in the response to transcranial magnetic brain stimulation in the general population. Clin Neurophysiol. 2002;113(7):1165–1171.
31. Stokes MG, Chambers CD, Gould IC, Henderson TR, Janko NE, Allen NB, Mattingley JB. Simple metric for scaling motor threshold based on scalp-cortex distance: application to studies using transcranial magnetic stimulation simple metric for scaling motor threshold based on scalp-cortex distance: application to studies using transcranial. J Neurophysiol. 2005;94(6):4520–4527.
32. Peterchev AV, Wagner TA, Miranda PC, Nitsche MA, Paulus W, Lisanby SH, Pascual-Leone A, Bikson M. Fundamentals of transcranial electric and magnetic stimulation dose: Definition, selection, and reporting practices. Brain Stimul. 2012;5(4):435–453.
33. Neggers SF, Petrov PI, Mandija S, Sommer IE, van den Berg NA. Understanding the biophysical effects of transcranial magnetic stimulation on brain tissue: the bridge between brain stimulation and cognition. Prog Brain Res. 2015;222: 229–259.
34. Sack AT, Cohen Kadosh R, Schuhmann T, Moerel M, Walsh V, Goebel R. Optimizing functional accuracy of TMS in cognitive studies: a comparison of methods. J Cogn Neurosci. 2009;21(2):207–221.
35. Thielscher A, Opitz A, Windhoff M. Impact of the gyral geometry on the electric field induced by transcranial magnetic stimulation. Neuroimage. 2011;54(1): 234–243.
36. Laakso I, Hirata A, Ugawa Y. Effects of coil orientation on the electric field induced by TMS over the hand motor area. Phys Med Biol. 2014;59(1): 203–218.
37. Krieg TD, Salinas FS, Narayana S, Fox PT, Mogul DJ. Computational and experimental analysis of TMS-induced electric field vectors critical to neuronal activation. J Neural Eng. 2015:12(4):1–11.
38. Paffi A, Camera F, Carducci F, Rubino G, Tampieri P, Liberti M, Apollonio F. A computational model for real-time calculation of electric field due to transcranial magnetic stimulation in clinics. Int J Antennas Propag. 2015;2015:1–12.
39. Janssen AM, Oostendorp TF, Stegeman DF. The coil orientation dependency of the electric field induced by TMS for M1 and other brain areas. J Neuroeng Rehabil. 2015;12:47.
40. Geddes LA, Baker LE. The specific resistance of biological material-a compendium of data for the biomedical engineer and physiologist. Med Biol Eng. 1967; 5(3):271–293.
41. Latikka J, Kuurne T, Eskola H. Conductivity of living intracranial tissues. Phys Med Biol. 2001;46(6):1611–1616.
42. Wagner TA, Zahn M, Grodzinsky AJ, Pascual-Leone A. Three-dimensional head model simulation of transcranial magnetic stimulation. IEEE Trans Biomed Eng. 2004;51(9):1586–1598.
43. Wagner T, Fregni F, Eden U, Ramos-Estebanez C, Grodzinsky A, Zahn M, Pascual-Leone A. Transcranial magnetic stimulation and stroke: a computer-based human model study. Neuroimage. 2006;30(3):857–870.
44. Opitz A, Windhoff M, Heidemann RM, Turner R, Thielscher A. How the brain tissue shapes the electric field induced by transcranial magnetic stimulation. Neuroimage. 2011;58:849–859.
45. Wenger C, Salvador R, Basser PJ, Miranda PC. The electric field distribution in the brain during TTFields therapy and its dependence on tissue dielectric properties and anatomy: a computational study. Phys Med Biol. 2015;60(18):7339–7357.
46. Opitz A, Fox MD, Craddock RC, Colcombe S, Milham MP. An integrated framework for targeting functional networks via transcranial magnetic stimulation. Neuroimage. 2016;157:86–96.
47. Peyman A, Gabriel C, Grant EH, Vermeeren G, Martens L. Variation of the dielectric properties of tissues with age: the effect on the values of SAR in children when exposed to walkie-talkie devices. Phys Med Biol. 2009;54(2):227–241.
48. Miranda PC, Hallett M, Basser PJ. The electric field induced in the brain by magnetic stimulation: a 3-D finite-element analysis of the effect of tissue heterogeneity and anisotropy. IEEE Trans Biomed Eng. 2003;50(9):1074–1085.
49. Oh SH, Lee BI, Lee SY, Woo EJ, Cho MH, Kwon O, Seo JK. Magnetic resonance electrical impedance tomography at 3 Tesla field strength. Magn Reson Med. 2004;51(6):1292–1296.
50. Zhang X, Yan D, Zhu S, He B. Noninvasive imaging of head-brain conductivity profiles using magnetic resonance electrical impedance imaging. IEEE Eng Med Biol Mag. 2008;27(5):78–83.
51. Woo EJ, Seo JK. Magnetic resonance electrical impedance tomography (MREIT) for high resolution conductivity imaging. Physiol Meas. 2008;29(10):R1–R26.
52. Seo JK, Yoon JR, Woo EJ, Kwon O. Reconstruction of conductivity and current density images using only one component of magnetic field measurements. IEEE Trans Biomed Eng. 2003;50(9):1121–1124.
53. Ider YZ, Onart S. Algebraic reconstruction for 3D magnetic resonance-electrical impedance tomography (MREIT) using one component of magnetic flux density. Physiol Meas. 2004;25(1):281–294.
54. Ozparlak L, Ider YZ. Induced current magnetic resonance–electrical impedance tomography. Physiol Meas. 2005;26(2):S289–S305.

55. van Lier ALHMW, van den Berg CAT, Katscher U. Measuring electrical conductivity at low frequency using the eddy currents induced by the imaging gradients. Paper presented at ISMRM 20th Annual Meeting; May 2012; Melbourne, Australia.
56. Liu C, Li W, Argyridis I. Imaging electric conductivity and conductivity anisotropy via eddy currents induced by pulsed field gradients. Paper presented at ISMRM 22nd Annual Meeting; May 2014; Milan, Italy.
57. Oran OF, Gurler N, Ider YZ. Feasibility of conductivity imaging based on slice selection and readout gradient induced eddy-currents. Paper presented at ISMRM 23rd Annual Meeting; June 2015; Toronto, Canada.
58. Gibbs E, Liu C. Feasibility of imaging tissue electrical conductivity by switching field gradients with MRI. Tomography. 2015;1(2):125–135.
59. Oran OF, Ider YZ. Feasibility of conductivity imaging using subject eddy currents induced by switching of MRI gradients. Magn Reson Med. 2016. doi: 10.1002/mrm.26283. [Epub ahead of print].
60. Mandija S, van Lier ALHMW, Katscher U, Petrov PI, Neggers SFW, Luijten PR, van den Berg CAT. A geometrical shift results in erroneous appearance of low frequency tissue eddy current induced phase maps. Magn Reson Med. 2015;76(3):905–912.
61. Schavemaker P, Sluis L van der. Electrical Power System Essentials. Chichester, England: John Wiley and Sons Inc.; 2008:238–240.
62. Laakso I, Hirata A. Fast multigrid-based computation of the induced electric field for transcranial magnetic stimulation. Phys Med Biol. 2012;57(23):7753–7765.
63. Hernandez-Garcia L, Bhatia V, Prem-Kumar K, Ulfarsson M. Magnetic resonance imaging of time-varying magnetic fields from therapeutic devices. NMR Biomed. 2013;26(6):718–724.
64. Institute S. SCIRun: A Scientific Computing Problem Solving Environment, Scientific Computing and Imaging Institute (SCI). 2015. http://www.scirun.org.
65. Petrov PI, Mandija S, van den Berg CAT, Neggers SFW. Impact of TMS coil modeling detail on FEM simulation accuracy of the induced electrical field. Paper presented at International Conference on Basic and Clinical Multimodal Imaging; September 2015; Utrecht, The Netherlands.
66. Miniussi C, Paulus W, Rossini PM. Transcranial Brain Stimulation. Boca Raton, FL: CRC Press Taylor & Francis Group; 2012:3—40.
67. Geuzaine C, Remacle JF. Gmsh: a three-dimensional finite element mesh generator with built-in pre- and post-processing facilities. Int J Numer Methods Eng. 2009;79:1309–1331.
68. Windhoff M, Opitz A, Thielscher A. Electric field calculations in brain stimulation based on finite elements: an optimized processing pipeline for the generation and usage of accurate individual head models. Hum Brain Mapp. 2013;34(4):923–935.
69. Mandija S, Petrov P, Neggers B, de Weijer A, Luijten PR, Van Den Berg CAT. MR guidance of TMS for a patient specific treatment plan: MR based TMS field measurements and electromagnetic simulations. Paper presented at ISMRM 23rd Annual Meeting; May 2015; Toronto, Canada.
70. Miranda PC. Physics of effects of transcranial brain stimulation. In: Lozano AM, Hallett M, eds. Handbook of Clinical Neurology, Elsevier; 2013;116:353–366.
71. Foster K. Dielectric properties of tissues. In: Bronzino JD, ed. The Biomedical Engineering Handbook. 2nd ed. Boca Raton: CRC Press; 2000.
72. Kim HJ, Jeong WC, Sajib SZK, Kim MO, Kwon OI, Je Woo E, Dong Hyun K. Simultaneous imaging of dual-frequency electrical conductivity using a combination of MREIT and MREPT. Magn Reson Med. 2014;71(1):200–208.
73. De Geeter N, Crevecoeur G, Dupré L, Van Hecke W, Leemans A. A DTI-based model for TMS using the independent impedance method with frequency-dependent tissue parameters. Phys Med Biol. 2012;57(8):2169–2188.
74. Navarro De Lara LI, Windischberger C, Kuehne A, Woletz M, Sieg J, Bestmann S, Weiskopf N, Strasser B, Moser E, Laistler E. A novel coil array for combined TMS[Sweta]fMRI experiments at 3 T. Magn Reson Med. 2015;74(5):1492–1501.